THE RECENT H_{α} VARIATIONS OF γ Cas

Y. NAZÉ^{1,2}, G. RAUW¹, E. BRYSSINCK³, X. DUPONT⁴, J. GUARRO FLO⁵

- 1) Groupe d'Astrophysique des Hautes Energies, STAR, Université de Liège, B5c, Allée du 6 Août 19c, B-4000 Sart Tilman, Liège, Belgium
 - 2) F.R.S.-FNRS Senior Research Associate ynaze@uliege.be
 - 3) BRIXIIS Observatory (MPC B96), Eyckensbeekstraat 2, 9150 Kruibeke, Belgium
 - 4) 4 rue de l'Orée du Bois, 37390 Saint-Roch, France
 - 5) Piera Remote Observatory, C. de Jaume Balmes 2, 08784 Piera (Barcelona), Catalonia

Abstract: First massive star reported to display Balmer emission lines, γ Cas has long served as a prototype for the Be category. Its bright and hard X-ray emission, however, makes it atypical amongst Be stars. In 2024-2025, an optical monitoring was undertaken in parallel to an X-ray campaign. Here we report on the results of this monitoring and we also derived refined ephemerides for the system combining $> 10^4$ d of radial velocity data.

1 Introduction

The fame of γ Cas (HD 5394, B0.5IVe) started in 1866 when Secchi (1866) reported the detection of Balmer emission lines in its optical spectrum. This led to the definition of the Be star category, which now gathers thousands of objects (see e.g. the BeSS database, Neiner et al. 2011). These optical emissions are now understood as being born in the decretion disk surrounding the star (for a review, see Rivinius et al. 2013). Such disks are not static: they build and dissipate, with variation timescales of days to decades. Being bright and considered as a Be prototype, γ Cas has benefitted from a constant attention from astronomers, professional as well as amateurs, so that its history is well known, with a disk dissipation followed by particularly active phases about a century ago (Baade et al., 2023). More recently, an enhanced disc activity took place around January 2021 (Rauw et al., 2022). In addition, γ Cas is also well known to be a binary, with SB1 orbital solutions calculated by several authors (Nemravová et al., 2012; Smith et al., 2012; Rauw et al., 2022), but it was also proposed to be a higher multiplicity system (e.g. Mamajek 2017).

What is less known is that γ Cas is actually atypical amongst Be stars when it comes to its high-energy emission. X-ray observations indeed reveal hard and bright emissions, corresponding to ultra-hot ($\sim 10\,\mathrm{keV}$) plasma (for a review, see Smith et al. 2016). Only about 10% of Be stars share such properties (Nazé & Robrade, 2023), making γ Cas the prototype of a subclass of Be stars, the γ Cas analogs. The origin of these X-rays remains debated, which is why new X-ray campaigns are regularly organized. In 2024-2025, such a campaign used the XRISM facility from the Japanese Space Agency. Simultaneously, a new optical campaign was set up and this paper aims at reporting its results. Section 2 describes the used data, Section 3 provides their analysis, and Section 4 summarizes the results and concludes this paper.

ISSN 1801-5964

October 2025

2 Observations

 γ Cas is a prominent target for a mateur astronomers. Three of them (co-authors Bryssinck, Dupont, Guarro-Flo) agreed to participate to a long γ Cas-centered campaign. The target was observed from mid-2024 to mid-2025, with 65 spectra taken to cover the H α line. All these spectra can be downloaded from the collective BeSS open-access database (Neiner et al. 2011 and http://basebe.obspm.fr). Each a mateur has its own instrument and its own observatory location hence the data were taken in various conditions. The used telescopes had diameters between 11 and 16 inches and spectrographs with resolving powers between 8500 and 15000. Exposure times ranged from 2 to 25 min, usually splitted into several subexposures. All data are of good quality (signal-to-noise ratios of at least 100 in nearly all spectra). The cadence was set to at least one spectrum per month and usually once per week, with more data taken around the dates of the X-ray observations. In the end, weather permitting, between 1 and 16 spectra per month are available over the duration of the campaign.

The first reduction steps (bias correction, flat field, wavelength calibration) were performed locally by each amateur in a standard way using various softwares (Audela, ISIS or SpecInti). In addition, a correction for telluric lines contamination was done within IRAF using the template of Hinkle et al. (2000). Normalization was finally performed using low degree polynomials through a chosen set of continuuum windows.

Several measurements were made on the H α line. First, moments up to third order were evaluated. The 0th-order moment is $M_0 = \sum f_i$ where f_i is the normalized flux (minus one) at wavelength λ_i ; it gives an idea of the equivalent width of the line (EW, after multiplication of M_0 by minus the step size in order to get a value in Å which is negative for emissions). The first-order moment estimates the centroid of the line: it is calculated following $M_1 = \sum f_i v_i / M_0$ where v_i is the velocity corresponding to wavelength λ_i (after barycentric correction). The second- and third-order moments are $M_2 = \sum f_i(v_i - v_i)$ $M_1)^2/M_0$ and $M_3 = \sum f_i(v_i - M_1)^3/M_0$, respectively. The square root of the former provides an idea of the line width, w, while the latter helps deriving the line skewness using $s = M_3/M_2^{1.5}$. Moments were evaluated between $-450 \,\mathrm{km \, s^{-1}}$ and $+450 \,\mathrm{km \, s^{-1}}$, with $\lambda_{ref} = 6562.85$ Å. In addition, the radial velocities (RVs) were also calculated using the mirror and double-Gaussian methods (see details in Nazé et al. 2022). The first-order moment considers the full line profile, but the line center is often very variable: the line wings, sensitive to disk areas closer to the star, are better suited to evaluate the true velocity of the Be star hence the additional use of two other methods. The mirror method finds the velocity shift at which the red and blue wings (after reversing the velocities of the blue one) best superimpose (Nemravová et al., 2012). Here, we considered wings with normalized fluxes between 2.0 and 3.7. The double-Gaussian method finds the velocity shift at which the correlation between the observed profile and a shifted model profile (consisting of two Gaussians with identical widths but opposite amplitudes) reaches zero (Smith et al., 2012). Here, we used Gaussians centered on $\pm 200 \,\mathrm{km}\,\mathrm{s}^{-1}$ with widths of $15 \,\mathrm{km}\,\mathrm{s}^{-1}$; correlation was done over the same velocity range as for the moment derivation.

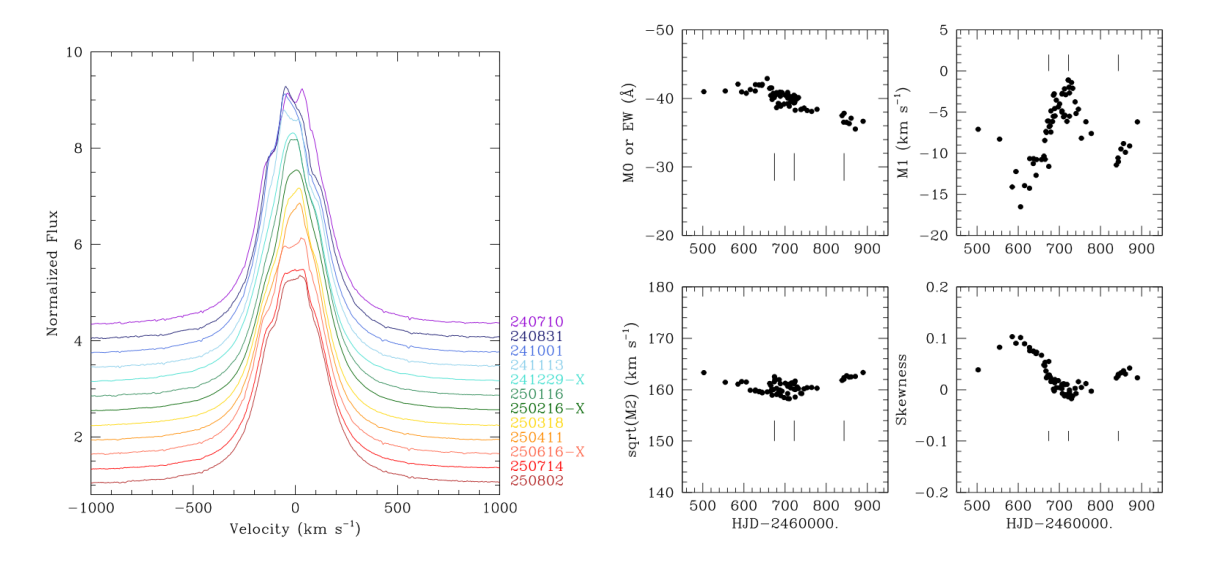


Figure 1: Evolution of the line profile and moments of the H α line of γ Cas during 2024-2025. X on the left panel and tickmarks in the right panel indicate times of the X-ray observations.

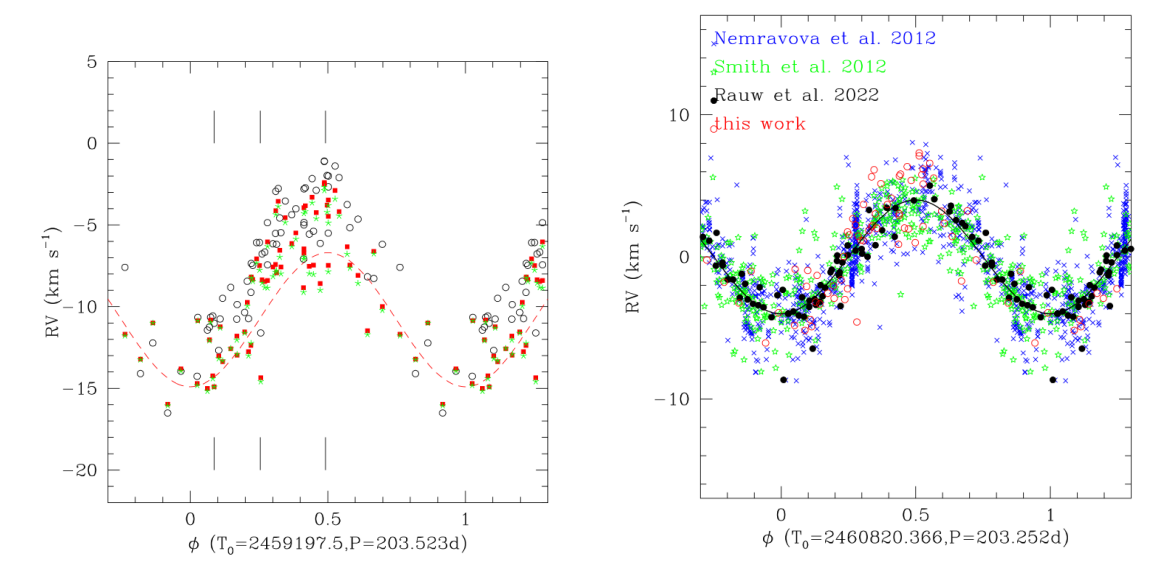


Figure 2: Left: Radial velocities of γ Cas during our campaign measured using the first order moment (black circles), mirror method (red squares), and double-Gaussian method (green stars) along with the best-fit orbital solution from Rauw et al. (2022). Right: Best-fit orbital solution combining all published RVs (for our RVs and those of Rauw et al. 2022, the values derived from the double-Gaussian method are shown).

Table 1: Characteristics of the H α line observed for γ Cas in 2024-2025 (see text for details). For those calculations, the line profile was considered in the interval $\pm 450 \mathrm{km} \, \mathrm{s}^{-1}$.

				Interval ±450		-1.
HJD $-2.4e6$	$M_0(ext{Å})$	$M_1(\mathrm{km}\mathrm{s}^{-1})$	$\sqrt{M_2} (\mathrm{km s}^{-1})$	Skewness	RV(km)	2G
60502.451	-40.99 ± 0.01	-7.08 ± 0.07	163.33 ± 0.06	0.038 ± 0.002	-8.8	-9.1
60554.440	-41.08 ± 0.01	-8.27 ± 0.05	161.46 ± 0.04	$0.082 {\pm} 0.001$	-6.6	-6.8
60585.281	-42.09 ± 0.01	-14.10 ± 0.04	161.08 ± 0.03	0.103 ± 0.001	-13.2	-13.2
60594.414	-40.96 ± 0.01	-12.22 ± 0.05	161.57 ± 0.04	0.090 ± 0.002	-11.0	-11.0
60605.429	-40.76 ± 0.01	-16.51 ± 0.06	161.50 ± 0.05	0.101 ± 0.002	-16.0	-16.1
60615.219	-41.28 ± 0.01	-13.95 ± 0.06	159.89 ± 0.05	0.089 ± 0.002	-13.8	-13.9
60627.242	-41.07 ± 0.01	-14.26 ± 0.06	159.76 ± 0.05	0.082 ± 0.002	-14.7	-14.8
60627.706	-42.01 ± 0.01	-10.66 ± 0.05	159.93 ± 0.04	0.076 ± 0.002	-10.9	-10.9
60636.323	-41.98 ± 0.01	-11.25 ± 0.08	159.63 ± 0.07	0.075 ± 0.003	-12.0	-12.1
60637.218	-41.94 ± 0.01	-10.65 ± 0.04	159.65 ± 0.04	0.075 ± 0.001	-10.8	-11.0
60643.198	-41.92 ± 0.01	-12.68 ± 0.09 -10.76 ± 0.04	159.54 ± 0.08 159.38 ± 0.04	0.070 ± 0.003	-13.0	-13.2
60644.219 60656.579	-42.05 ± 0.01 -42.89 ± 0.01	-10.76 ± 0.04 -10.76 ± 0.04	159.55 ± 0.04 159.55 ± 0.04	0.073 ± 0.001 0.067 ± 0.001	-11.2 -11.8	-11.3 -12.0
60662.395	-42.89 ± 0.01 -41.45 ± 0.01	-10.76 ± 0.04 -10.35 ± 0.05	161.20 ± 0.04	0.048 ± 0.001	-11.5	-12.6
60664.311	-41.43 ± 0.01 -41.52 ± 0.01	-8.44 ± 0.04	159.65 ± 0.03	0.048 ± 0.002 0.047 ± 0.001	-9.7	-10.0
60665.233	-40.44 ± 0.01	-10.73 ± 0.04	160.81 ± 0.03	0.053 ± 0.001	-12.8	-13.0
60667.241	-41.52 ± 0.01	-7.35 ± 0.04	160.01 ± 0.04	0.036 ± 0.001	-8.2	-8.2
60668.393	-39.86 ± 0.01	-7.47 ± 0.03	158.92 ± 0.03	0.023 ± 0.001	-8.3	-8.4
60671.216	-40.75 ± 0.01	-6.08 ± 0.04	160.01 ± 0.03	0.027 ± 0.001	-7.1	-7.3
60673.395	-40.14 ± 0.01	-6.07 ± 0.04	161.54 ± 0.03	0.028 ± 0.001	-7.5	-7.8
60674.290	-40.48 ± 0.01	-11.61 ± 0.05	162.53 ± 0.04	0.055 ± 0.001	-14.3	-14.6
60675.272	-40.57 ± 0.01	-6.77 ± 0.04	162.06 ± 0.04	0.029 ± 0.001	-8.4	-8.5
60677.262	-40.53 ± 0.01	-6.66 ± 0.05	161.97 ± 0.04	0.025 ± 0.001	-8.5	-8.8
60679.287	-40.85 ± 0.01	-4.86 ± 0.04	160.27 ± 0.03	0.022 ± 0.001	-6.0	-6.3
60679.307	-38.65 ± 0.01	-7.44 ± 0.04	159.08 ± 0.03	0.016 ± 0.001	-8.4	-8.9
60683.349	-39.28 ± 0.01	-6.15 ± 0.06	159.40 ± 0.05	0.017 ± 0.002	-7.6	-8.1
60685.215	-39.20 ± 0.01	-5.52 ± 0.07	159.35 ± 0.06	0.018 ± 0.002	-7.4	-7.9
60685.397	-40.57 ± 0.01	-2.95 ± 0.05	161.96 ± 0.04	0.001 ± 0.002	-4.1	-4.4
60687.255	-40.92 ± 0.01	-2.77 ± 0.03	159.93 ± 0.03	-0.002 ± 0.001	-3.5	-3.9
60688.344	-40.32 ± 0.01	-4.57 ± 0.04	161.18 ± 0.04	0.014 ± 0.001	-6.5	-7.0
60689.218	-38.86 ± 0.01	-5.47 ± 0.04	158.82 ± 0.04	0.020 ± 0.001	-7.6	-8.0
60692.423	-40.86 ± 0.01	-3.54 ± 0.03	159.72 ± 0.03	0.004 ± 0.001	-4.6	-4.8
60697.244 60700.295	-39.18 ± 0.01 -40.46 ± 0.01	-4.37 ± 0.05	158.48 ± 0.05	0.017 ± 0.002 0.004 ± 0.001	-6.1 -5.5	-6.3 -5.9
60706.238	-39.23 ± 0.01	-4.01 ± 0.05 -5.00 ± 0.04	161.24 ± 0.04 158.31 ± 0.04	0.004 ± 0.001 0.009 ± 0.001	-5.5 -6.5	-3.9 -7.0
60706.291	-40.88 ± 0.01	-3.00 ± 0.04 -2.79 ± 0.03	159.27 ± 0.04 159.27 ± 0.03	0.009 ± 0.001 0.002 ± 0.001	-3.9	-4.3
60706.296	-40.07 ± 0.01	-4.85 ± 0.04	160.69 ± 0.03	0.010 ± 0.001	-6.7	-7.1
60707.265	-40.54 ± 0.01	-2.72 ± 0.05	161.04 ± 0.04	-0.007 ± 0.002	-3.8	-4.2
60710.232	-38.87 ± 0.01	-5.56 ± 0.04	158.26 ± 0.04	0.012 ± 0.001	-7.5	-8.0
60712.301	-40.02 ± 0.01	-2.16 ± 0.04	160.98 ± 0.04	-0.012 ± 0.001	-3.3	-3.6
60713.307	-39.51 ± 0.01	-5.39 ± 0.03	160.34 ± 0.03	0.010 ± 0.001	-7.5	-8.0
60715.343	-40.23 ± 0.01	-2.88 ± 0.05	161.32 ± 0.04	-0.010 ± 0.001	-4.2	-4.6
60718.344	-39.73 ± 0.01	-6.13 ± 0.04	161.36 ± 0.04	0.010 ± 0.001	-8.6	-9.0
60721.318	-40.48 ± 0.01	-1.11 ± 0.03	160.12 ± 0.03	-0.010 ± 0.001	-2.4	-2.7
60721.321	-39.32 ± 0.01	-1.09 ± 0.04	161.16 ± 0.03	-0.014 ± 0.001	-2.5	-2.9
60723.333	-39.41 ± 0.01	-1.97 ± 0.05	161.50 ± 0.04	-0.008 ± 0.001	-3.8	-4.2
60724.241	-38.29 ± 0.01	-5.50 ± 0.06	158.58 ± 0.05	-0.001 ± 0.002	-7.5	-7.9
60724.323	-40.30 ± 0.01	-2.00 ± 0.04	160.05 ± 0.03	-0.010 ± 0.001	-3.5	-3.8
$60724.339 \\ 60729.275$	-39.68 ± 0.01 -39.94 ± 0.01	-2.67 ± 0.05 -1.39 ± 0.03	161.69 ± 0.04 160.52 ± 0.03	-0.005 ± 0.001 -0.017 ± 0.001	-4.5 -2.9	-4.9 -3.4
60732.283	-39.94 ± 0.01 -40.13 ± 0.01	-1.39 ± 0.03 -2.10 ± 0.03	160.32 ± 0.03 160.22 ± 0.03	-0.017 ± 0.001 -0.012 ± 0.001	-4.2	-3.4 -4.4
60738.266	-38.37 ± 0.01	-3.76 ± 0.08	159.29 ± 0.07	0.002 ± 0.001	-6.3	-6.8
60740.265	-38.43 ± 0.01	-5.16 ± 0.05	159.27 ± 0.05	-0.008 ± 0.002	-7.5	-7.6
60746.282	-38.60 ± 0.01	-4.64 ± 0.04	160.18 ± 0.04	0.016 ± 0.001	-8.1	-8.6
60753.279	-38.23 ± 0.01	-8.17 ± 0.04	160.40 ± 0.04	0.004 ± 0.001	-11.5	-11.7
60764.282	-38.11 ± 0.01	-6.18 ± 0.05	160.45 ± 0.04	0.012 ± 0.002	-10.0	-10.2
60777.318	-38.42 ± 0.01	-7.59 ± 0.07	160.28 ± 0.06	-0.003 ± 0.002	-11.7	-11.8
60838.366	-37.50 ± 0.01	-11.43 ± 0.06	161.83 ± 0.06	0.023 ± 0.002	-15.0	-15.2
60842.362	-36.53 ± 0.01	-10.57 ± 0.07	161.98 ± 0.06	$0.026 {\pm} 0.002$	-14.2	-14.4
60843.377	-37.84 ± 0.01	-11.02 ± 0.05	162.35 ± 0.04	0.030 ± 0.002	-14.9	-14.9
60849.616	-36.51 ± 0.01	-9.49 ± 0.03	162.73 ± 0.03	0.033 ± 0.001	-13.4	-13.3
60855.616	-36.31 ± 0.01	-8.82 ± 0.04	162.44 ± 0.03	0.037 ± 0.001	-12.6	-12.6
60860.374	-37.11 ± 0.01	-9.87 ± 0.07	162.50 ± 0.06	0.031 ± 0.002	-13.0	-12.9
60870.572	-35.54 ± 0.01	-9.12 ± 0.04	162.59 ± 0.04	0.042 ± 0.001	-12.4	-12.2
60889.517	-36.68 ± 0.01	-6.18 ± 0.04	163.34 ± 0.04	0.023 ± 0.001	-7.9	-7.8

Table 2: Same as Table 1 but for our previous TIGRE campaign (Rauw et al., 2022).

	table 2. Same					
HJD	$M_0(\text{\AA})$	$M_1 ({\rm km s^{-1}})$	$\sqrt{M_2} (\mathrm{km}\mathrm{s}^{-1})$	Skewness	$RV(\mathrm{km})$	
-2.4e6					mirror	2G
58626.969	-40.74 ± 0.01	-8.49 ± 0.02	162.67 ± 0.02	0.043 ± 0.001	-10.7	-10.8
58650.954	-40.86 ± 0.01	-6.43 ± 0.02	163.09 ± 0.02	0.010 ± 0.001	-7.5	-7.6
58670.908	-41.88 ± 0.01	-5.67 ± 0.03	164.07 ± 0.02	0.014 ± 0.001	-7.2	-7.4
58696.810	-41.09 ± 0.01	-4.62 ± 0.03	163.52 ± 0.02	-0.007 ± 0.001	-5.8	-5.8
58712.761	-39.99 ± 0.01	-5.51 ± 0.02	164.16 ± 0.02	-0.013 ± 0.001	-7.0	-7.3
58728.788	-39.63 ± 0.01	-7.11 ± 0.02	163.98 ± 0.01	0.002 ± 0.001	-9.2	-9.5
58743.728	-40.84 ± 0.01	-8.30 ± 0.02	165.00 ± 0.02	0.018 ± 0.001	-11.5	-11.5
58760.704	-40.53 ± 0.01	-9.19 ± 0.02	165.20 ± 0.02	0.022 ± 0.001	-12.7	-12.8
58771.599	-40.81 ± 0.01	-9.12 ± 0.02	164.90 ± 0.02	0.006 ± 0.001	-12.9	-13.0
58803.636	-40.27 ± 0.01	-8.89 ± 0.03	165.02 ± 0.02	-0.001 ± 0.001	-13.4	-13.7
58817.614	-40.25 ± 0.01	-7.96 ± 0.02	165.59 ± 0.02	-0.010 ± 0.001	-12.7	-12.8
58831.624	-40.94 ± 0.01	-7.14 ± 0.02	165.91 ± 0.01	-0.013 ± 0.001	-12.0	-12.2
58848.624	-40.78 ± 0.01	-5.74 ± 0.02	165.87 ± 0.01	-0.020 ± 0.001	-10.2	-10.3
58867.615	-39.10 ± 0.02	-4.04 ± 0.14	164.99 ± 0.11	-0.019 ± 0.004	-7.7	-7.4
58992.966	-41.57 ± 0.01	-15.93 ± 0.02	167.97 ± 0.02	0.077 ± 0.001	-19.2	-19.5
59014.965	-42.06 ± 0.01	-14.88 ± 0.02	166.53 ± 0.02	0.092 ± 0.001	-17.0	-17.3
59035.973	-43.22 ± 0.01	-12.58 ± 0.02 -12.58 ± 0.02	166.36 ± 0.02 166.36 ± 0.02	0.092 ± 0.001 0.090 ± 0.001	-13.9	-14.3
59076.876	-43.22 ± 0.01 -44.95 ± 0.01	-12.38 ± 0.02 -11.79 ± 0.02	165.55 ± 0.02	0.083 ± 0.001	-9.3	-9.4
59106.732	-44.50 ± 0.01 -45.50 ± 0.01	-10.60 ± 0.02	162.97 ± 0.02	0.089 ± 0.001	-6.9	-6.8
59100.732	-45.30 ± 0.01 -47.02 ± 0.01	-10.00 ± 0.02 -11.22 ± 0.03	162.97 ± 0.02 161.49 ± 0.02	0.089 ± 0.001 0.086 ± 0.001	-8.6	
						-8.5
59145.580	-47.84 ± 0.01	-11.66 ± 0.02	161.38 ± 0.02	0.075 ± 0.001	-9.5	-9.2
59164.616	-47.18 ± 0.01	-12.94 ± 0.03	159.94 ± 0.02	0.090 ± 0.001	-12.3	-12.1
59191.547	-47.44 ± 0.01	-13.02 ± 0.01	158.01 ± 0.01	0.066 ± 0.001	-13.7	-13.6
59195.539	-47.21 ± 0.01	-12.56 ± 0.01	158.04 ± 0.01	0.060 ± 0.001	-13.3	-13.2
59199.539	-47.36 ± 0.01	-14.16 ± 0.01	158.02 ± 0.01	0.065 ± 0.001	-15.1	-14.9
59203.604	-47.52 ± 0.01	-13.04 ± 0.02	158.05 ± 0.01	0.082 ± 0.001	-14.8	-14.7
59207.605	-47.78 ± 0.01	-13.15 ± 0.01	158.63 ± 0.01	0.071 ± 0.001	-15.3	-15.0
59211.606	-48.27 ± 0.01	-12.65 ± 0.01	159.11 ± 0.01	0.063 ± 0.001	-15.2	-15.1
59215.597	-47.72 ± 0.01	-12.06 ± 0.01	159.00 ± 0.01	0.049 ± 0.001	-14.6	-14.4
59219.597	-47.79 ± 0.01	-10.56 ± 0.01	159.66 ± 0.01	0.057 ± 0.001	-14.0	-13.8
59223.634	-47.59 ± 0.01	-9.89 ± 0.02	160.17 ± 0.01	0.051 ± 0.001	-14.0	-14.0
59227.645	-47.21 ± 0.01	-9.34 ± 0.02	160.25 ± 0.01	0.037 ± 0.001	-13.2	-13.0
59232.550	-46.21 ± 0.01	-7.65 ± 0.01	160.42 ± 0.01	0.026 ± 0.001	-11.7	-11.8
59236.552	-46.22 ± 0.01	-6.74 ± 0.02	161.01 ± 0.02	0.018 ± 0.001	-11.1	-11.1
59240.573	-45.79 ± 0.01	-6.96 ± 0.04	160.42 ± 0.04	0.007 ± 0.001	-11.4	-11.3
59244.568	-46.00 ± 0.01	-5.52 ± 0.01	160.70 ± 0.01	0.010 ± 0.001	-9.9	-10.1
59255.558	-46.43 ± 0.01	-6.40 ± 0.02	160.51 ± 0.01	0.004 ± 0.001	-10.5	-10.6
59259.559	-45.27 ± 0.01	-6.65 ± 0.02	159.91 ± 0.01	0.004 ± 0.001	-10.8	-10.8
59265.560	-45.46 ± 0.01	-6.02 ± 0.01	160.95 ± 0.01	0.003 ± 0.001	-10.0	-10.0
59270.562	-44.59 ± 0.01	-5.18 ± 0.01	161.30 ± 0.01	-0.007 ± 0.001	-9.0	-9.0
59418.922	-41.45 ± 0.01	-11.70 ± 0.02	165.20 ± 0.01	0.059 ± 0.001	-14.0	-13.9
59423.913	-41.42 ± 0.01	-12.14 ± 0.04	164.71 ± 0.04	0.051 ± 0.001	-14.1	-14.2
59428.900	-41.70 ± 0.01	-11.75 ± 0.02	165.11 ± 0.01	0.041 ± 0.001	-13.6	-13.6
59434.881	-41.56 ± 0.01	-10.22 ± 0.02	164.57 ± 0.01	0.032 ± 0.001	-11.8	-11.9
59441.847	-40.93 ± 0.01	-10.79 ± 0.02	163.54 ± 0.02	0.021 ± 0.001	-11.7	-11.9
59447.829	-41.89 ± 0.01	-8.13 ± 0.05	163.76 ± 0.04	0.032 ± 0.001	-10.6	-10.7
59453.805	-41.34 ± 0.01	-7.87 ± 0.02	163.69 ± 0.01	0.020 ± 0.001	-10.4	-10.4
59497.777	-41.53 ± 0.01	-3.93 ± 0.01	165.58 ± 0.01	-0.004 ± 0.001	-6.8	-6.9
59524.691	-39.83 ± 0.01	-5.09 ± 0.01	165.57 ± 0.01	0.005 ± 0.001	-7.7	-7.7
59529.610	-40.49 ± 0.01	-5.89 ± 0.01	165.89 ± 0.01	-0.006 ± 0.001	-8.3	-8.3
59536.631	-39.66 ± 0.01	-5.99 ± 0.01	165.49 ± 0.01	0.010 ± 0.001	-8.7	-8.7
59546.608	-39.72 ± 0.01	-7.14 ± 0.01	165.97 ± 0.01	0.007 ± 0.001	-9.7	-9.7
59551.595	-39.52 ± 0.01	-8.44 ± 0.01	165.38 ± 0.01	0.026 ± 0.001	-11.5	-11.5
59556.619	-39.53 ± 0.01	-8.32 ± 0.01	165.55 ± 0.01	0.024 ± 0.001	-11.2	-11.3
59560.613	-39.03 ± 0.01	-9.47 ± 0.01	165.13 ± 0.01	0.024 ± 0.001	-12.4	-12.5
59564.595	-38.95 ± 0.01	-9.31 ± 0.01	165.11 ± 0.01	0.037 ± 0.001	-12.4	-12.5
59569.622	-39.39 ± 0.01	-10.75 ± 0.01	165.39 ± 0.01	0.047 ± 0.001	-13.8	-13.7
59575.559	-39.11 ± 0.01	-10.95 ± 0.01	165.34 ± 0.01	0.038 ± 0.001	-13.7	-13.9
59579.554	-39.04 ± 0.01	-11.36 ± 0.01	165.49 ± 0.01	0.040 ± 0.001	-14.1	-14.2
59583.563	-39.19 ± 0.01	-11.66 ± 0.01	165.49 ± 0.01	0.039 ± 0.001	-14.1	-14.3
59587.586	-38.98 ± 0.01	-11.43 ± 0.01	165.78 ± 0.01	0.053 ± 0.001	-14.2	-14.4
59593.567	-38.79 ± 0.01	-11.90 ± 0.01	165.78 ± 0.01	0.053 ± 0.001	-14.9	-15.1
59606.571	-39.14 ± 0.01	-11.79 ± 0.01	165.97±0.01	0.047 ± 0.001	-14.7	-14.8

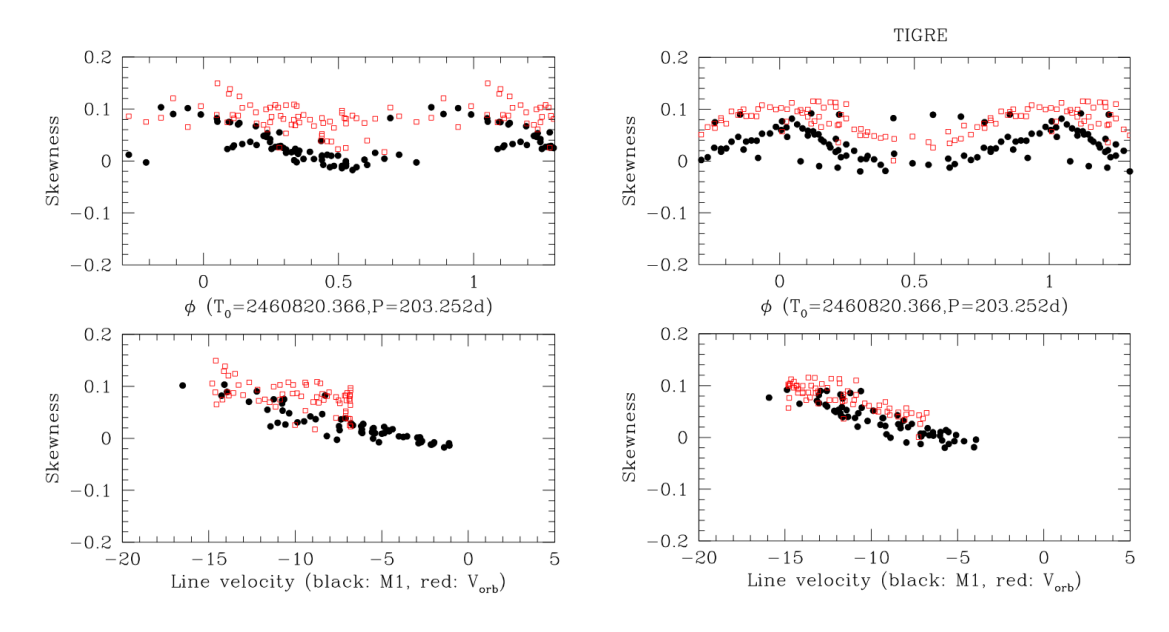


Figure 3: Skewness vs orbital phase or line velocity, for our new campaign (left) or the previous TIGRE campaign (right, Rauw et al. 2022).

3 Results

Table 1 provides the moments and RVs calculated for the spectra of this campaign. Note that the 1- σ errors on the moments are calculated from error propagation using the signal-to-noise ratios of the spectra: they actually are too optimistic - e.g. a more typical uncertainty on M_1 is 2km s^{-1} . Figure 1 shows the evolution of the H α line profile and of its four moments over the campaign duration. During our previous campaign (Rauw et al., 2022), the strength of H α rose up during an enhanced activity episode lasting several months ($\Delta EW \sim 10\text{Å}$). After that, the line strength decreased back to its initial value. During this new campaign, EW started at a similar level as the "base" one of the previous monitoring and then the line strength slowly declined ($\Delta EW \sim 6\text{Å}$). The line width w remained quite stable near 160km s^{-1} , although with a shallow trend of increasing width with decreasing line strength (an anticorrelation already reported in Rauw et al. 2022 and which is usual for an inside-out dissipation of the disk).

As shown in Fig. 2, the RV obtained from the various methods agree quite well, with a higher dispersion seen from the core-contaminated M_1 values, as usual. Keeping the orbital period fixed to $203.523\,\mathrm{d}$, the best sinusoidal fit yields $\gamma = -9.9 \pm 0.4\mathrm{km\,s^{-1}}$, $K = 4.6 \pm 0.5\mathrm{km\,s^{-1}}$, and $T_0 = 2\,460\,615.571 \pm 2.7$ (with T_0 corresponding to a quadrature with a minimum RV value). Long-term variations may change the zero point (Nemravová et al., 2012) but the RV amplitude K does agree well with that previously derived for γ Cas (Rauw et al., 2022). However, the reference time appears slightly offset in phase ($\Delta\phi \sim 0.03$) from the T_0 of Rauw et al. (2022). A similar difference had already been reported in that paper when comparing its T_0 value with those of Nemravová et al. (2012), indicating a slightly overestimated period. To improve the period value, we therefore decided to combine all available RVs, i.e. those from Smith et al. (2012), Nemravová et

OPEN EUROPEAN JOURNAL ON VARIABLE STARS

https://oejv.physics.muni.cz

DOI: 10.5817/OEJV2025-0266 October 2025 ISSN 1801-5964

al. (2012), Rauw et al. (2022) - see Table 2, and ours (Table 1). This combined dataset covers an interval of nearly 12000 days. To avoid any long-term disturbance in the combined dataset, we first fitted each RV subset by a sinusoid, deriving the best γ and we then subtracted this value from the associated RVs before combining them with the others. Next, we performed a period search and a global sinusoid fitting of the whole set of RVs. The new ephemerides for γ Cas are: $T_0 = 2460820.366 \pm 1.823$ (corresponding to a RV minimum), $P = 203.252 \pm 0.356 d$, and $K = 4.01 \pm 0.09 km s^{-1}$ (Fig. 2). This yields a mass function $f(m) = 0.00136 \pm 0.00009 \,\mathrm{M}_{\odot}$: for a system inclination of 42° (Stee et al., 2012) and a primary mass of 13 or $16 \,\mathrm{M}_{\odot}$, the secondary mass would then be 0.96 or $1.10 \,\mathrm{M}_{\odot}$, corresponding to mass ratios $q = M_2/M_1 = 0.074$ or 0.069.

Figure 1 also shows an intriguing trend: the skewness appears in opposition of phase with the line centroid M_1 , hence with the velocity of the Be star. This indicates an extended red wing when the Be lines are blueshifted (or blue wing if redshifted). To be sure that this effect is real, we re-calculated second and third order moments using as reference "mean" velocity the expected velocity from the above ephemerides rather than M_1 . This avoids biases due to core emission variability which can plague the M_1 determination. The trend appears to remain (Fig. 3). Furthermore, we calculated moments from our previous campaign (Table 2), in the classical way as well as considering the expected RV from the orbital solution. While the disk exhibited a different state, the skewness/velocity trend remains the same (Fig. 3). A last check considered the possibility of a calculation bias. Indeed, the selected velocity interval is fixed, i.e. it does not depend on the Be star motion. This leads to a small truncation of the line profile, on the blue side when the line is blueshifted (red side if redshifted). We therefore estimated moments for a line composed of two Gaussians (σ of 3.2 and 10Å, amplitudes of 4.3 and 0.4, respectively), a combination which reproduces the overall line profile well. This "fake" line was shifted following the above orbital solution and the observed velocity-skewness trend was then reproduced. If the velocity interval is enlarged, the trend becomes shallower, as could be expected. This indicates that the effect is not real, i.e. intrinsic to the system's behaviour, but a simple mathematical artifact.

Summary 4

In this paper, we report on an optical observing campaign performed on γ Cas from mid-2024 to mid-2025. We estimated moments and RVs of the H α line. While remaining strong, the Be disk appeared to be slowly dissipating over the campaign duration. By combining our new RVs with published ones, we improved the ephemerides of this important system.

Acknowledgements: This work has made use of the ADS, Simbad, and BeSS databases.

OPEN EUROPEAN JOURNAL ON VARIABLE STARS

https://oejv.physics.muni.cz

October 2025 DOI: 10.5817/OEJV2025-0266 ISSN 1801-5964

References

- Baade, D., Labadie-Bartz, J., Rivinius, T., et al. 2023, A&A, 678, 2023A&A...678A...47B
- Hinkle, K., Wallace, L., Valenti, J., & Harmer, D. 2000, Visible and Near Infrared Atlas of the Arcturus Spectrum 3727-9300 A ed. Kenneth Hinkle, Lloyd Wallace, Jeff Valenti, and Dianne Harmer. (San Francisco: ASP) ISBN: 1-58381-037-4, 2000. 2000vnia.book.....H
- Mamajek, E. 2017, Journal of Double Star Observations, 13, 2, 264 2017JDSO...13..264M
- Nazé, Y., Rauw, G., Czesla, S., et al. 2022a, MNRAS, 510, 2286 2022MNRAS.510.2286N
- Nazé, Y. & Robrade, J. 2023, MNRAS, 525, 3, 4186 <u>2023MNRAS.525.4186N</u>
- Neiner, C., de Batz, B., Cochard, F., et al. 2011, AJ, 142, 149 <u>2011AJ....142..149N</u>
- J., Harmanec, P., Koubský, P., et al. 2012, A&A, 537, A59 2012A&A...537A..59N
- Rauw, G., Nazé, Y., Motch, C., et al. 2022, A&A, 664, A184 2022A&A...664A.184R
- Rivinius, T., Carciofi, A. C., & Martayan, C. 2013, A&ARv, 21, 69 2013A&ARv..21...69R
- Secchi, A. 1866, Astronomische Nachrichten, 68, 63 1866AN.....68...63S
- Smith, M. A., Lopes de Oliveira, R., Motch, C., et al. 2012, A&A, 540, A53 2012A&A...540A..53S
- Smith, M. A., Lopes de Oliveira, R., & Motch, C. 2016, Advances in Space Research, 58, 5, 782 2016AdSpR..58..782S
- Stee, P., Delaa, O., Monnier, J. D., et al. 2012, A&A, 545, A59 <u>2012A&A...545A..59S</u>